

# **Co<sub>3</sub>O<sub>4</sub>-Al<sub>2</sub>O<sub>3</sub> Mesoporous Hollow Spheres as Efficient Catalyst for Fischer-Tropsch Synthesis**

Xin-Pu Fu<sup>a</sup>, Qi-Kai Shen<sup>a</sup>, Dong Shi<sup>a</sup>, Ke Wu<sup>c</sup>, Zhao Jin<sup>a</sup>, Xu Wang<sup>b</sup>, Rui Si<sup>\*.b</sup>, Qi-Sheng Song<sup>a</sup>,

Chun-Jiang Jia<sup>\*.a</sup>, Chun-Hua Yan<sup>\*.c</sup>

<sup>a</sup>Key Laboratory for Colloid and Interface Chemistry, Key Laboratory of Special Aggregated Materials, School of Chemistry and Chemical Engineering, Shandong University, Jinan 250100, China

<sup>b</sup>Shanghai Synchrotron Radiation Facility, Shanghai Institute of Applied Physics, Chinese Academy of Sciences, Shanghai 201204, China

<sup>c</sup>Beijing National Laboratory for Molecular Sciences, State Key Lab of Rare Earth Materials Chemistry and Applications, PKU-HKU Joint Lab in Rare Earth Materials and Bioinorganic Chemistry, Peking University, Beijing 100871, China

## **Abstract**

Nanostructured mixed metal oxides with porous hollow-interior structure hold great promise in environmental-related catalysis, owing to their excellent catalytic properties. However, facile fabrication of such mesoporous architecture is still challenging. Here, by using a transient aerosol-assisted self-assembly (AASA) method, we synthesized the  $\text{Co}_3\text{O}_4\text{-Al}_2\text{O}_3$  mesoporous hollow spheres (MHS) composed of thermally stable  $\text{Co}_3\text{O}_4$  nanoparticles partially anchored to amorphous interfacial  $\text{Al}_2\text{O}_3$ . The as-prepared  $\text{Co}_3\text{O}_4\text{-Al}_2\text{O}_3$  nanocomposites displayed distinct features of large pore volume and stable assembled morphology, and thus showed significant advantages in mass transfer and redox behavior. For Fischer-Tropsch synthesis, a very important reaction in fuel production, the  $\text{Co}_3\text{O}_4\text{-Al}_2\text{O}_3$  MHS exhibited significant catalytic performance in conversion, selectivity and stability for the desired gasoline products. Therefore, we provide a facile and controlled approach towards the preparation of mesoporous hollow materials to achieve novel mixed metal oxide nanocatalysts those are good candidates in energy-production application.

**Keywords:** Mesoporous Hollow Spheres; Mixed Metal Oxide; Interfacial Structure; Aerosol-Assisted Self-Assembly; Fischer-Tropsch Synthesis

## 1. Introduction

Diverse carbon sources such as coal, nature gas and biomass, can be converted to syn-gas, and thus the Fischer-Tropsch Synthesis (FTS) reaction,<sup>[1-11]</sup> one of the key technologies to produce environmentally oil, has attracted special research interests for the energy production of synthetic fuels those are ultra-clean and particularly compatible with current vehicle. Among various catalysts used in FTS reaction, porous metal oxides (PMO) display impressive catalytic performance and have become increasingly attractive on account of the their abundant porosity, high surface area and unique surface-interface structure.<sup>[12-17]</sup> It has been well known that as the particle size of active component decreases to less than 10 nm, catalyst can exhibit significantly enhanced reactivity ascribed to the exposure of significant amount of active sites. However, small nanoparticles tend to be severely sintered and quickly lose the catalytic reactivity under harsh reaction conditions. In the past decade, researchers have used thermally stable secondary metal oxide as a structural stabilizer to resolve such problems for the wider applications of nanosized PMO. Many strategies such as sol-gel,<sup>[12,13]</sup> chemical etching,<sup>[18,19]</sup> co-assembly approach<sup>[14,20]</sup> and so forth, have been carried out to obtain thermally stable mixed metal oxides nanocomposites. Up to date, it is still challenging to achieve the rational design of interfacial nanostructure via controllable approach for anchoring active nanoparticles, which not only has interaction with the stabilizer, but also plays crucial roles in optimizing the related catalytic performance.<sup>[21]</sup>

Among various assembled nanostructures of PMO, hollow spheres draw manifold interest in chemistry due to their low specific weight, high storage capacity and tunable surface properties.<sup>[18,22-29]</sup> One typical route towards such hollow nanostructure is the hard-template method, i. e. the solid skeletons<sup>[18,23,25]</sup> (silica, polystyrene spheres, carbon and metal ions, etc.) are removed from the corresponding core-shell precursors via a calcination or etching step. Other routes including Oswald ripening<sup>[25]</sup>, Kirkendall process,<sup>[26,27]</sup> decomposition of metal-organic frameworks<sup>[28]</sup> or coordination polymers<sup>[29]</sup> and so forth, can be classified as assembly approaches, and have also been successfully applied. Although many strategies have been established to derive mesoporous hollow

architecture with stable morphology in nanoscale, most of them are limited by their complicated synthesis processes.

In this work, by the aids of transient pyrolysis process of metal nitrate, we developed a facile synthesis of thermally stable  $\text{Co}_3\text{O}_4\text{-Al}_2\text{O}_3$  mesoporous hollow spheres (MHS) via an aerosol-assisted self-assembly (AASA) approach<sup>[30–33]</sup>. To our best knowledge, binary metal oxides of hollow structure without the use of any template have been seldom fabricated before. Herein the hollow interior of  $\text{Co}_3\text{O}_4\text{-Al}_2\text{O}_3$  MHS was formed during a self-induced process. Specifically, the crystallization of  $\text{Co}_3\text{O}_4$  nanoparticles was accompanied by the release of gaseous  $\text{N}_x\text{O}_y$  from metal precursor. Furthermore, due to the remarkable structural and textural properties, this  $\text{Co}_3\text{O}_4\text{-Al}_2\text{O}_3$  MHS displays moderately interfacial interaction and excellent mass transfer ability, thus inducing much superior performance for Fischer-Tropsch synthesis (FTS) reaction. Compared with conventionally solid catalysts, greatly higher CO conversion, as well as the much superior selectivity on desired  $\text{C}_5\text{--C}_{12}$  products has been confirmed for  $\text{Co}_3\text{O}_4\text{-Al}_2\text{O}_3$  MHS during the catalytic tests. Therefore, this facile strategy may have great significance in the fields of both material science and energy-related catalysis.

## 2. Experimental

### 2.1. Catalyst preparation

**2.1.1 Material.** All materials were purchased from commercial vendors and used without further modifications or purification. Cobalt nitrate ( $\text{Co}(\text{NO}_3)_2 \cdot 6\text{H}_2\text{O}$ ), aluminum nitrate ( $\text{Al}(\text{NO}_3)_3 \cdot 9\text{H}_2\text{O}$ ) and citric acid ( $\text{C}_6\text{H}_8\text{O}_7$ ) were purchased from Tianjin Kernal Chemical Reagent Factory. Triblock copolymer, (ethylene oxide)<sub>106</sub>-(propylene oxide)<sub>70</sub>-(ethylene oxide)<sub>106</sub> (Pluronic F127,  $M_w = 12,000 \text{ g} \cdot \text{mol}^{-1}$ ) and  $\text{EO}_{20}\text{PO}_{70}\text{EO}_{20}$  (Pluronic P123,  $M_n = 5,800$ ) were purchased from Sigma-Aldrich.

**2.1.2 Preparation of  $\text{Co}_3\text{O}_4\text{-Al}_2\text{O}_3$  mesoporous hollow spheres.** As the Scheme 1 shown, the  $\text{Co}_3\text{O}_4\text{-Al}_2\text{O}_3$  mesoporous hollow spheres were synthesized by an AASA method. First, triblock copolymer Pluronic F127 (0.8 g) was dissolved in pure ethanol (120 mL). After stirring for one hour, 8 mmol of mixed cobalt nitrate and aluminum nitrate (molar ratio of Co/Al is 70/30) were added into

the above solution. After 10 min stirring, the stock solution was then transferred to the household ultrasonic humidifier to produce microspheres via the aerosol-spraying process. The atomized spray was sequentially carried by pure N<sub>2</sub> flow (150 mL·min<sup>-1</sup>) through a 90 cm-length glass tube placed in a tube furnace at 450 °C. Finally, the as-formed powders were collected with a filter connected to a water aspirator and further calcined at 450 °C (ramp rate: 1 °C·min<sup>-1</sup>) for 6 h in still air. The as-prepared Co<sub>3</sub>O<sub>4</sub>-Al<sub>2</sub>O<sub>3</sub> hollow mesoporous spheres are labeled as 70Co\_MHS. Similarly, other Co<sub>3</sub>O<sub>4</sub>-Al<sub>2</sub>O<sub>3</sub> mesoporous solid spheres with different molar ratios of Co/Al (15/85, 30/70, 50/50, 90/10, 100/0) were synthesized and are labeled as xCo ( $x = 15, 30, 50, 90, 100$ ). To break the limitation of particular Co/Al ratio (7/3) for MHS, additional treatment (e.g. alkali etching) could be taken on the obtained sample.

The Co<sub>3</sub>O<sub>4</sub>-Al<sub>2</sub>O<sub>3</sub> sample was also prepared via a sol-gel method<sup>[5,6]</sup> and used as reference catalyst for Fischer-Tropsch Synthesis. First, 1.0 g of Pluronic P123 was dissolved in pure ethanol (20 mL) at room temperature. Then, citric acid (0.84 g) and appropriate quantities of Al(NO<sub>3</sub>)<sub>3</sub>·9H<sub>2</sub>O (6 mmol) and Co(NO<sub>3</sub>)<sub>2</sub>·6H<sub>2</sub>O (14 mmol) salts were added to the solution under vigorous stirring. The stock solution was continuously stirred at room temperature for 5 h, and sequentially transferred into a drying oven to undergo the solvent evaporation at 60 °C for another two days. The as-formed gel was calcined in still air at 450 °C (ramp rate: 1 °C·min<sup>-1</sup>) for 4 h to obtain the final product.

Another reference catalyst was prepared by impregnation route with 20wt. % Co loading (20Co\_IM). The matrix of mesoporous alumina was synthesized via a sol-gel method used above, which the metal salt was only Al(NO<sub>3</sub>)<sub>3</sub>·9H<sub>2</sub>O (8 mmol). Then, the obtained matrix was fully grinding and dispersed in 30 mL deionized water by ultrasonic treatment for 30 min. Subsequently, the appropriate quantities of Co(NO<sub>3</sub>)<sub>2</sub>·6H<sub>2</sub>O salts were added to the solution under vigorous stirring for another 30 min and then evaporated at 80 °C with stirring. The as-formed powders were further dried in an oven for 12 h. Finally, the sample was calcined in air at 450 °C (ramp rate: 1 °C·min<sup>-1</sup>) for 4 h to obtain the final product.

## 2.2 Characterization.

*Ex-situ* X-ray diffraction (XRD) was conducted on a PANalytical B.V. X'pert3 powder diffractometer (40 kV, 40 mA), using Cu  $K\alpha_1$  radiation ( $\lambda = 0.15406$  nm). The diffraction patterns were collected at room temperature with a step of  $0.01^\circ$  and an accumulation time of 30 s for each step. The *in-situ* XRD was performed on the same machine with an Anton Paar XRK-900 reaction chamber. For monitoring the phase transformation during H<sub>2</sub>-TPR test, the samples were loaded into a ceramic sample holder (diameter = 10 mm, depth = 1 mm) and then heated up from room temperature to 800 °C in 5% H<sub>2</sub>/Ar. Two scans with ca. 20 min for each were collected at each testing temperature (25 °C, 200 °C, 350 °C, 600 °C and 800 °C). To determine the phase transformation of catalysts during FTS reaction, the powders were loaded into a ceramic sample holder and then heated up to 350 °C for 10 h in 5% H<sub>2</sub>/Ar, then kept at 220 °C in syn-gas (33.3% CO/H<sub>2</sub>) for another 10 h with XRD pattern collection.

The H<sub>2</sub>-TPR tests were carried out in a Builder PCSA-1000 instrument (Beijing, China) equipped with a thermal conductivity detector (TCD) to detect H<sub>2</sub> consumption. The fresh catalysts (ca. 30 mg, 20–40 mesh) were pre-treated at 350 °C in air (0.5 h). Following cooled to room temperature, the sample was flushed using pure N<sub>2</sub> at room temperature for about 30 min, then switched to 10 % H<sub>2</sub>/Ar and heated from room temperature to 900 °C with a ramping rate of 5 °C min<sup>-1</sup>.

The degree of reduction (DOR) of catalysts were determined by another programmed reduction tests, in which the catalyst were heated from 20 °C to 350 °C with a ramping rate of 10 °C min<sup>-1</sup> and then were maintained at 350 °C for another 10 h. Subsequently, the temperature continued increased to 900 °C with a ramping rate of 10 °C min<sup>-1</sup>. The DOR values were calculated based on ratio of the H<sub>2</sub> consumed area before 350 °C to the total consumed area during 30–900 °C.

Transmission electron microscopy (TEM) and high-resolution TEM (HRTEM) were conducted on a Philips Tecnai F20 instrument operating at 200 kV. All the investigated samples were sonicated in ethanol before being dropped on an ultra-thin carbon film-coated Cu grid. For the corresponding elemental mapping, energy dispersive spectroscopy (EDS) was applied to the measured samples under the scanning transmission electron microscopy (STEM) mode on the same machine.

Scanning electron microscope (SEM) was taken on a Zeiss SUPRA 55 scanning microscope with an acceleration voltage of 5.0 kV.

X-ray photoelectron spectroscopy (XPS) characterization was carried out on an Axis Ultra XPS spectrometer (Kratos, UK) with 225 W of Al  $K\alpha$  radiation. The C  $1s$  peak at 284.8 eV was used as the internal calibration.

The N<sub>2</sub>-sorption measurement was operated in a Builder SSA-4200 physic-sorption analyzer at 77 K after degassing process at 200 °C for 6 h under vacuum. The BET specific surface areas were calculated by the experimental data from 0.05 to 0.20  $P/P_0$ .

X-ray absorption fine structure (XAFS) spectra at Co  $K$ -edge ( $E_0 = 7709$  eV) were collected at BL14W1 beamline of the Shanghai Synchrotron Radiation Facility (SSRF), with the storage ring being operated at 3.5 GeV under constant currents of 220 mA (“top-up” mode). The XAFS data were collected under transmission mode with ion chambers. The energy was calibrated according to the absorption edge of pure Co foil. Athena and Artemis codes were used to extract the data and fit the profiles.<sup>[34,35]</sup> For the X-ray absorption near edge structure (XANES) part, the experimental absorption coefficients as function of energies  $\mu(E)$  were processed by background subtraction and normalization procedures, and reported as “normalized absorption”. Based on the comparison with standards (Co foil, CoO and Co<sub>3</sub>O<sub>4</sub>), the oxidation state of each sample was determined. For the extended X-ray absorption fine structure (EXAFS) part, the Fourier transformed (FT) data in R space were analyzed by applying bulk Co, CoO and Co<sub>3</sub>O<sub>4</sub> for Co-O and Co-Co shells. The passive electron factors,  $S_0^2$ , were determined by fitting the experimental Co foil data and fixing the Co-Co coordination number (CN) to be 12, and then fixed for further analysis of the measured samples. The parameters describing the electronic properties (e.g., correction to the photoelectron energy origin,  $E_0$ ) and local structure environment including CN, distance ( $R$ ) and Debye Waller (D.W.) factor around the absorbing atoms were allowed to vary during the fit process.

### 2.3 Catalytic test.

The Fischer-Tropsch synthesis reaction was conducted using a fixed-bed flow reactor with a gas mixture of 32% CO, 64% H<sub>2</sub>, and 4% N<sub>2</sub>. The measurements at different temperature were

carried out under 2 MPa after a pretreatment at 350 °C for 10 h in 10% H<sub>2</sub>/Ar flow by 2 °C/min rate and the flow rate is 50.4 mL·min<sup>-1</sup>. 80 mg catalyst mixed with 420 mg quartz sand (20–40 mesh) was tested at 220 °C and the data was collected at time on stream of 5 h. The stability test for 70 h on 70Co\_MHS was taken at the same reaction conditions and the results were collected every 10 h. The products and reactants in the gas phase were detected online by using two tandem gas chromatography (Shanghai-Ouhua GC-9160). C<sub>1</sub>–C<sub>4</sub> ranged hydrocarbons were analyzed using a Plot Al<sub>2</sub>O<sub>3</sub> capillary column with a flame ionization detector (FID); CO, CO<sub>2</sub>, CH<sub>4</sub>, and N<sub>2</sub> were analyzed by using a Porapak Q and 5A molecular sieve-packed column with a thermal conductivity detector (TCD). To calculate the CO conversion, the 4% N<sub>2</sub> in the syngas was used as an internal standard. The selectivity of the products was all on a carbon basis. The selectivity CO<sub>2</sub> was calculated according to all the used CO, and the selectivity of CH<sub>4</sub>, C<sub>2</sub>–C<sub>4</sub> or C<sub>5+</sub> was based on all the produced hydrocarbons.

All the spent catalysts were cooled down to room temperature in N<sub>2</sub> gas, then switch to diluted O<sub>2</sub> (1%O<sub>2</sub>/Ar) for half an hour. To try to passivate the surface of used catalysts, we immediately transferred all the investigated samples after FTS into vials and filled them with N<sub>2</sub> gas before the corresponding characterizations (XRD, XPS and XAFS).

### **3. Results and Discussion**

#### **3.1 Structural and Textural Properties of Co<sub>3</sub>O<sub>4</sub>-Al<sub>2</sub>O<sub>3</sub> MHS**

In this work, Co<sub>3</sub>O<sub>4</sub>-Al<sub>2</sub>O<sub>3</sub> MHS was prepared by an AASA method as demonstrated in Scheme 1. Specifically, an ethanol solution of mixed metal nitrates and surfactant (F127) were atomized using an ultrasonic humidifier and then was transported into a preheated (450 °C) tube oven by continuous N<sub>2</sub> carrier. During this transient process, the growth and self-assembly of metal oxides were accompanied by the evaporation of ethanol. Subsequently, the powder product was gathered by a collector and the sequential calcination step was conducted at 450 °C in still air to remove the added surfactants (please refer to Experimental Section).



The scanning electron microscopy (SEM) image in Figure 1a displays that 70Co\_MHS has an integrated spherical morphology with a diameter of 100–600 nm. As revealed by the transmission electron microscopy (TEM) image in Figure 1b, the sharp contrast between the shell and the interior cavity identifies the morphology of hollow spheres. Furthermore, by using the line energy-dispersive X-ray spectroscopy (EDS) analysis (Figure 1c), we determined the changes of chemical compositions in as-prepared 70Co\_MHS, which identifies the hollow structure for both Co and Al species.

To get insight into the primary structure of hollow spheres, we thoroughly grounded the powders sample to determine the morphology of crushed 70Co\_MHS. Figure 1d exhibits that the spherical shells are composed by uniformly small-size ( $8.5\pm 1.7$  nm in average) particles. Figure 1e verifies the presence of highly crystallized nanoparticles with *d*-spacing of 0.29 and 0.24 nm, in good agreement with those of (220) and (311) planes in Co<sub>3</sub>O<sub>4</sub>, respectively. According to the STEM-EDS elemental mapping results in Figure 1f, we confirmed that both cobalt and aluminum species are homogeneously dispersed in the primary particles. The crystal structure of 70Co\_MHS was examined by powder X-ray diffraction (XRD). Figure 2a displays that all the diffraction peaks can be indexed to cubic Co<sub>3</sub>O<sub>4</sub> phase (JCPDS card no 73–1701), in good agreement with HRTEM images, and no detectable Al<sub>2</sub>O<sub>3</sub> or other Al-containing structure, suggesting the amorphous nature of Al<sub>2</sub>O<sub>3</sub> after 450 °C air-calcination.

The Co 2*p* XPS measurement was carried out to detect the interaction between Co and Al species in 70Co\_MHS. Figure 2b shows two deconvoluted peaks located at 779.8 and 781.8 eV for Co 2*p*<sub>3/2</sub>. Due to the specific interval of 15.0 eV between Co 2*p*<sub>1/2</sub> and Co 2*p*<sub>3/2</sub>, the major contribution at 779.8 eV can be attributed to Co<sub>3</sub>O<sub>4</sub>.<sup>[36,37]</sup> However, the other peak located at 781.8 eV, which is 1.6 eV higher than the typical B.E. of CoO (780.2 eV) and 2.0 eV higher than that of Co<sub>3</sub>O<sub>4</sub>, was detected. This component cannot be assigned to bulk CoAl<sub>2</sub>O<sub>4</sub> or CoO either, because there is no obvious satellite observed.<sup>[36]</sup> Thus, the component at 781.8 eV could be assigned to interfacial cobalt species interacted with Al<sub>2</sub>O<sub>3</sub>, which might be formed during the calcination process<sup>[36]</sup>.

The textural and porous properties of  $\text{Co}_3\text{O}_4\text{-Al}_2\text{O}_3$  hollow structure were measured by the  $\text{N}_2$  adsorption-desorption experiment. Figure S1 apparently displays the H2 hysteresis loop of 70Co\_MHS can be attributed to the mesoporous nanomaterials.<sup>[38]</sup> As shown in Table 1, 70Co\_MHS shows a BET surface area of  $95 \text{ m}^2\cdot\text{g}^{-1}$  and one larger pore volume of  $0.61 \text{ cm}^3\cdot\text{g}^{-1}$  than other samples with solid nature, which consequently induced a large expose area of Co sites and one excellent mass transfer ability. Therefore, as discussed above, the as-prepared hollow spheres have mesoporous architecture with both Co and Al accumulations in the outside shell. The highly crystallized fraction is composed by small-size  $\text{Co}_3\text{O}_4$  nanoparticles, which are efficiently confined by bits interfacial  $\text{Al}_2\text{O}_3$ .

### 3.2 Formation Mechanism on $\text{Co}_3\text{O}_4\text{-Al}_2\text{O}_3$ MHS

To investigate the formation of  $\text{Co}_3\text{O}_4\text{-Al}_2\text{O}_3$  MHS, we intentionally adjusted the experimental parameters during the AASA synthesis.

First, we found that the ratio of Co/Al play an important role on controlling the morphology of as-prepared products. The SEM images in Figure S2 exhibit that all the  $\text{Co}_3\text{O}_4\text{-Al}_2\text{O}_3$  samples have a spherical architecture, but the surface roughness clearly increases with the Co/Al ratio. The corresponding TEM images in Figure 3 reveal that no hollow structure similar to 70Co\_MHS can be verified for other ratios of 15Co, 30Co, 50Co and 100Co, which all display the solid interiors. From Figures S3d-S3f, we observed that 50Co was consisted of uniform highly crystallized  $\text{Co}_3\text{O}_4$  particles with an average size of  $7.9\pm 1.7 \text{ nm}$ , and the slight amorphous alumina species were dispersed around the cobalt oxide phase with the similar interfacial structure to 70Co\_MHS (Figure 1d). However, without any Al, 100Co was composed by non-uniform  $\text{Co}_3\text{O}_4$  particles (see Figures S3g-S3i). Furthermore, once the Co/Al molar ratio decreases to 30/70 (Figure S3b), the  $\text{Co}_3\text{O}_4$  nanoparticles were surrounded by abundant alumina. Thus, the addition of  $\text{Al}_2\text{O}_3$  effectively tuned the growth of cobalt oxide grains and stabilized the uniform small-size  $\text{Co}_3\text{O}_4$  nanoparticles. We also noticed the existence of plenty of voids inside the solid spheres (see Figure 3d), indicating that

amorphous alumina species act as adhesives to connect the  $\text{Co}_3\text{O}_4$  nanocrystals to form integrate spheres.

Second, the textural properties of different  $\text{Co}_3\text{O}_4\text{-Al}_2\text{O}_3$  nanocomposites were tested by  $\text{N}_2$  adsorption-desorption experiments. Figure S1 displays the hysteresis loops for all the samples, which confirms their mesoporous architecture nature.<sup>[38]</sup> From Table 1, we could distinctly verify the decrease of BET values ( $231 \text{ m}^2/\text{g} \rightarrow 28 \text{ m}^2/\text{g}$ ) with the increase of Co/Al ratio ( $15\text{Co} \rightarrow 100\text{Co}$ ), revealing that the lighter alumina has higher surface area than the relatively heavier cobalt oxide. However, for pore volume (Table 1), 70Co\_MHS shows a significant improved number of  $0.61 \text{ cm}^3\cdot\text{g}^{-1}$ , much larger than those with other Co/Al ratios ( $0.27\text{--}0.34 \text{ cm}^3\cdot\text{g}^{-1}$ ), well consistent with the largest hysteresis loop for 70Co\_MHS on isotherm adsorption/desorption curves (Figure S1). These results on porosity demonstrate that Co/Al = 70/30 is indispensable to derive mesoporous hollow spheres in  $\text{Co}_3\text{O}_4\text{-Al}_2\text{O}_3$  system.

Third, we further investigated the intermediate  $\text{Co}_3\text{O}_4\text{-Al}_2\text{O}_3$  mesoporous nanocomposites before air-calcination by SEM (Figure 4a), and also found the same hollow interior as final product. However, unlike 70Co\_MHS, the STEM-EDS line scanning (Figure 4b) and area mapping (Figure 4c) results identify the Co-Al core-shell structure for 70Co\_IM, although the crystallized phase is still  $\text{Co}_3\text{O}_4$  by XRD analysis (Figure 4d). Additionally, there was no N signal could be detected from the EDS result (Figure 4e), indicating the sufficient pyrolysis of nitrate precursor during the transient AASA process. These data obviously give hints on the fact that amorphous alumina species further diffused from interior to exterior in the post calcination (air,  $450 \text{ }^\circ\text{C}$ , 6 h) step, while the structural skeleton (uniform  $\text{Co}_3\text{O}_4$  nanocrystals) formed during the transmit pyrolysis process. So, the appropriate Co/Al ratio is the key factor to stabilize the  $\text{Co}_3\text{O}_4$  skeleton in our synthesis. Figures S4a (SEM) and 4b (STEM-EDS) describe that solid spheres with homogeneous distributions of both Co and Al appeared for the intermediate state of Co/Al = 30/70 (30Co\_IM), and thus no hollow structure was generated after the sequential air-calcination (STEM-EDS, Figure S4c). Meanwhile, if the alumina was dominant, the crystallization of cobalt oxide was severely prevented during the

AASA process and 30Co\_IM required further calcination step to obtain  $\text{Co}_3\text{O}_4$  nanocrystals (refer to XRD patterns in Figure S4d).

Therefore, on the basis of the above observations, the formation mechanism of our  $\text{Co}_3\text{O}_4\text{-Al}_2\text{O}_3$  mesoporous hollow sphere can be described as a facile self-induced process, as illustrated in Scheme 1. Initially, nitrate precursors ( $\text{Co}(\text{NO}_3)_2$  and  $\text{Al}(\text{NO}_3)_3$ ) were homogeneously dispersed in ethanol solution with moderate amount of surfactant (F127). Then, the stock solution volatilized in the hot  $\text{N}_2$  gas flow, and gaseous  $\text{N}_x\text{O}_y$  was released from the decomposition of metal precursors. Simultaneously, the structural skeleton (uniform  $\text{Co}_3\text{O}_4$  nanocrystals) formed at the exterior of sphere and amorphous alumina species adhered to the cobalt oxide shell. During the sequential air-calcination step, the residual  $\text{Al}_2\text{O}_3$  at the interior transferred to the architecture outside and the final mesoporous hollow sphere generated. We have also demonstrated that the appropriate concentrations of cobalt and aluminum salts are extremely important for us to obtain the integrate  $\text{Co}_3\text{O}_4\text{-Al}_2\text{O}_3$  MHS. If Co/Al ratio is too high (e.g. 100/0), non-uniform  $\text{Co}_3\text{O}_4$  nanoparticles will appear since no adhesive effect by  $\text{Al}_2\text{O}_3$ ; if Co/Al ratio is too low (e.g. 30/70), solid spheres with low pore volume (around  $0.3 \text{ cm}^3/\text{g}$ ) will form because not enough  $\text{Co}_3\text{O}_4$  nanocrystals can be used as structural skeleton. So, 70Co\_MHS is unique in this work.

Furthermore, without the addition of surfactant (F127), the hollow spheres were still created in preparation (Figure S5). However, the mesoporous features, e. g. large pore volume and big hysteresis loop in isotherm absorption/desorption curves, disappeared for the  $\text{Co}_3\text{O}_4\text{-Al}_2\text{O}_3$  nanocomposites (please see Table 1 and Figure S1 for details). Otherwise, as displayed in TEM image, the surface of 70Co without F127 was slightly collapsed compared with 70Co\_MHS. Thus, proper amount of F127 is necessary to produce the mesoporous channels and keep the hollow structure intact.

### 3.3 Catalytic Performance of $\text{Co}_3\text{O}_4\text{-Al}_2\text{O}_3$ MHS for Fischer-Tropsch Synthesis

Here, we used the Fischer-Tropsch synthesis (FTS), a very important industrial reaction for green gas-to-liquid (GTL) process,<sup>[39,40]</sup> as a model reaction to probe the catalytic properties of the as-prepared  $\text{Co}_3\text{O}_4\text{-Al}_2\text{O}_3$  samples. Up to now, much research has revealed the Co-based catalysts are

suitable for synthesis of long-chain hydrocarbons.<sup>[1,3]</sup> Hence, it has great demand to facilitate the fabrication of efficient Co-based catalysts with high stability and specific selectivity for oil products, especially for gasoline (C<sub>5</sub>–C<sub>12</sub>).

Firstly, we compared the 70Co\_MHS with other solid nanospheres (xCo). All the nanocomposites were used as catalysts in the Fischer-Tropsch synthesis reaction under the same condition (T = 220 °C, H<sub>2</sub>/CO = 2, P = 20 bar) which has been widely applied in many reports previously.<sup>[2,4]</sup> Before reaction, all the catalysts were *in-situ* reduced in 10% H<sub>2</sub> for 16 h and more detailed information about the FTS test is seen in the Experiment Section. Figure 5a and Table 2 show that under the same reaction conditions (T = 220 °C, m<sub>catal.</sub> = 80 mg, H<sub>2</sub>/CO = 2/1, 2.0 MPa, 10 mL·min<sup>-1</sup>, time-on-stream of 5 h), the hollow sphere of 70Co\_MHS exhibited one much superior CO conversion (65.7%) and reaction rate normalized by catalyst weight ( $r_{\text{FTS}} = 6.7 \times 10^{-2} \text{ mol}_{\text{CO}} \cdot \text{g}_{\text{cat}}^{-1} \cdot \text{h}^{-1}$ ) to the solid architecture of 15Co ~ 100Co (CO conversion: 3.7–65.7%;  $r_{\text{FTS}}$ : 0.4–4.3 × 10<sup>-2</sup> mol<sub>CO</sub>·g<sub>cat</sub><sup>-1</sup>·h<sup>-1</sup>). Meanwhile, as shown in Table 2 and Figure 5a, 70Co\_MHS also displayed the largest cobalt-time-yield (CTY) value of 3.51 × 10<sup>-5</sup> mol<sub>CO</sub>·g<sub>Co</sub><sup>-1</sup>·s<sup>-1</sup>, much better than other samples (0.20–2.91 × 10<sup>-5</sup> mol<sub>CO</sub>·g<sub>Co</sub><sup>-1</sup>·s<sup>-1</sup>). Furthermore, without alumina, the reactivity of 100Co vastly decreased to 0.2 × 10<sup>-5</sup> mol<sub>CO</sub>·g<sub>Co</sub><sup>-1</sup>·s<sup>-1</sup> (Figure 5a). It revealed that the interfacial Al<sub>2</sub>O<sub>3</sub> in 70Co\_MHS plays an important role for stabilization of active cobalt species. However, if the concentration of alumina was too high, the reactivity of 15Co and 30Co drastically dropped, probably due to the less exposure of active Co species. Additionally, Figure 5b shows that our 70Co\_MHS catalyst also exhibited obvious superiority in the selectivity (52.4%) for desired C<sub>5</sub>–C<sub>12</sub> products than the other solid spheres (14.3–46.2%). The optimized selectivity for long-chain hydrocarbons of such hollow materials was reconfirmed by the chain growth probability ( $\alpha$ ) that 70Co/Al\_MHS showed the highest  $\alpha$ -value character ( $\alpha = 0.82$ ) in all the measured catalysts (Figure S6). This obvious distinction in selectivity here might be ascribed to the size-effect in Co-based catalysts.<sup>[1,41]</sup>

Furthermore, based on previous reports, the convention level and the consequently water pressure always impact the selectivity of hydrocarbons.<sup>[42,43]</sup> Therefore, The CO conversion of

70Co\_MHS and other reference catalysts were tuned to be comparable by changing the Gas Hourly Space Velocity (GHSV) to compare the product selectivity. As the results shown in Table 2, the C<sub>5+</sub> selectivity of 70Co\_MHS slightly decreased (from 70.7 to 67.7%), in consistent with previous investigation that the added water can increase the C<sub>5+</sub> selectivity.<sup>[43]</sup> While, one much higher CTY value ( $5.5 \times 10^{-5} \text{ mol}_{\text{CO}} \cdot \text{g}_{\text{Co}}^{-1} \cdot \text{s}^{-1}$ ) of 70Co\_MHS was acquired under low conversion level, comparing with other catalysts, proving the superior performance of as-prepared hollow structured catalyst.

The 70Co\_MHS and 50Co have an average particle size of ~ 8 nm, which is optimized for FTS reaction as discussed above. While, no detectable diffraction peaks shown in the XRD pattern of 15Co, indicating the very small size of Co nanoparticles, which might be one factor to the low activity. For 30Co, the average diameter of Co nanoparticles determined by XRD pattern is about 9 nm, which is similar to that of 50Co and 70Co\_MHS. However, as shown in HRTEM image (Figure S3b), Co nanoparticles of 30Co were seriously coated by alumina. According to previous investigation, the less exposed Co species might increase the residence times of reversibly bonded CH<sub>x</sub> and OH<sub>x</sub> intermediates, thus which might lead to higher CH<sub>4</sub> selectivity of 15Co and 30Co.<sup>[44,45]</sup> Moreover, with similar structure of Co nanoparticles to 50Co, the 70Co\_MHS exhibited much higher degree of reduction (0.57) than that of 50Co (0.32), as well as better activity ( $5.5 \times 10^{-5}$  v.s.  $3.1 \times 10^{-5} \text{ mol}_{\text{CO}} \cdot \text{g}_{\text{Co}}^{-1} \cdot \text{s}^{-1}$ , Table 2) under similar conversion level (18–31%, Table 2), which might benefit from the hollow feature of 70Co\_MHS. Additionally, for the 15Co and 30Co, major Co species in the bulk of the spheres had strong interaction to ambient alumina were hardly reduced after pre-treatment. Thus, the 15Co and 30Co presented much lower activity than 70Co\_MHS.

The long-term stability test results in Figure 6a identify that the catalytic durability of 70Co\_MHS for FTS was very good up to 70 h, and only slight decrease on CO conversion (from 63 to 59%) was observed. For better comparison, we prepared another catalyst with less alumina (90Co, Co:Al = 9:1, Figure S8) and evaluated its deactivation behavior during 70 h test. As shown in Figure S9, the 90Co exhibited a great loss from ~ 60% to ~ 20% under FTS reaction, further proving the important role of the interfacial alumina in improving stability for 70Co\_MHS.

As mentioned above, for the catalyst of 50Co and 70Co\_MHS, they have similar cobalt particle

size of ~8 nm (Table 1), while diverse features in morphology (70Co MHS: Hollow, see Figure 1b; 50Co: Solid, see Figure 3c). However, as the result of having hollow structure, the 70Co\_MHS had more than two times higher pore volume than solid 50Co (0.60 v.s. 0.28 cm<sup>3</sup>/g), also much larger pore diameter (18.8 v.s. 6.3 nm), which greatly promoted the mass transfer ability with lots accessible mesoporous channels.<sup>[46–48]</sup> Moreover, the hollow spheres exhibited better reducibility than solid ones (DOR: 0.58 v.s. 0.32, see Table 1). Consequently, the more reduced hollow spheres exhibited one enhanced FTS performance (CTY, 5.5×10<sup>-5</sup> v.s. 3.1×10<sup>-5</sup> mol<sub>CO</sub>·g<sub>Co</sub><sup>-1</sup>·s<sup>-1</sup>, Table 2) than solid ones (50Co).

Furthermore, to exclude the interference of the various Co/Al ratios between 50Co and 70Co\_MHS, 70Co\_SG (prepared by sol-gel method, Co/Al = 7/3, Figure S10) with solid structure were prepared for further comparison. Owing to the hollow architecture, more cobalt species are present in the surface of 70Co\_MHS than the solid 70Co\_SG, which thus induced much higher degree of reduction (0.58 v.s. 0.25, Table 1). As shown in Figure 6b and Table 2, 70Co\_MHS not only showed superior activity in CO conversion (65.7%) and CTY (3.51×10<sup>-5</sup> mol<sub>CO</sub>·g<sub>Co</sub><sup>-1</sup>·s<sup>-1</sup>), more than three times (17.8% and 0.95×10<sup>-5</sup> mol<sub>CO</sub>·g<sub>Co</sub><sup>-1</sup>·s<sup>-1</sup>) of 70Co (sol-gel), but also exhibited the higher selectivity to desirable C<sub>5</sub>–C<sub>12</sub> hydrocarbons (52.4 vs 38%).

Another conventional catalyst prepared via the impregnation method with 20wt. % Co (20Co\_IM) was also used for further comparison with 70Co\_MHS. As the XRD spectrum shown in Figure S11, the major Co species of 20Co\_IM is Co<sub>3</sub>O<sub>4</sub> with a diameter of 7.3 nm (determined by XRD pattern). The 20Co\_IM also exhibits a similar DOR with 70Co\_MHS of ~57% (refer to Table 1). Subsequently, the 20Co\_IM was evaluated as catalyst for FTS reaction. As the results shown in Table 2, 20Co\_IM displayed almost same selectivity with 70Co\_MHS, which might be owing to the similar structure of Co nanoparticles of both catalysts.<sup>[41,42]</sup> However, the CTY of 20Co\_IM was much lower than 70Co\_MHS with one similar conversion level (1.6×10<sup>-5</sup> vs. 5.5×10<sup>-5</sup> mol<sub>CO</sub>·g<sub>Co</sub><sup>-1</sup>·s<sup>-1</sup>), which might attributing to the less homogeneous dispersion and solid feature of 20Co\_IM.

Therefore, on the basis of the above experimental evidences, we can draw a conclusion that, owing to the better mass transfer ability and higher content of exposed Co species, the hollow architecture effectively promoted the performance of the 70Co\_MHS in FTS reaction. And the current  $\text{Co}_3\text{O}_4\text{-Al}_2\text{O}_3$  mesoporous hollow sphere is a promising catalyst for the FTS reaction from all the aspects of activity, selectivity and stability. 70Co\_MHS distinctly showed its superiority to either solid catalysts with other Co/Al ratios or the 70Co\_SG with the same chemical composition but without the hollow structure.

### 3.4 Structural Evolution on $\text{Co}_3\text{O}_4\text{-Al}_2\text{O}_3$ MHS for FTS

As displayed in Figure 7, even after rough FTS reaction, 30Co and 70Co\_MHS still integrally preserved sphere architecture, indicating the fine structural stability of as-prepared nanocomposites. To be different with solid interior of spent 30Co, the 70Co\_MHS obviously showed mesoporous and hollow feature after FTS reaction. Conversely, when there was no amorphous alumina in this system (100Co), while the 100Co was seriously collapsed, confirming the good structural stability of as prepared hollow architecture.

As discussed above, compared to the  $\text{Co}_3\text{O}_4\text{-Al}_2\text{O}_3$  samples with other compositions, 70Co\_MHS exhibited superior catalytic performance for FTS. To identify the active species of Co-based catalysts, we used X-ray absorption fine structure (XAFS) technique to trace the structural evolution on different  $\text{Co}_3\text{O}_4\text{-Al}_2\text{O}_3$  nanocomposites before and after the reaction. XAFS which is elemental sensitive and very powerful to determine the electronic and local coordination structure of investigated metals. In X-ray near edge spectroscopy (XANES) region of XAFS, the edge energy, the white line intensity and the pre-edge features are related to the oxidation state of  $\text{Co}^{3+}/\text{Co}^{2+}/\text{Co}^0$ . Compared to XPS, which usually requires high level of vacuum, XANES can be conducted under milder ambient conditions. In extended X-ray absorption fine structure (EXAFS) part of XAFS, the short-range (up to 6–8 Å) coordination structural parameters (distance  $R$ , coordination number  $CN$ , etc.) can be obtained via the corresponding simulation with appropriate models.

The XANES profile in Figure 8a presents that the oxidation state of Co in 70Co\_MHS perfectly matches the  $\text{Co}_3\text{O}_4$  reference, indicating the combination of  $\text{Co}^{2+}$  and  $\text{Co}^{3+}$  species. From the Co K



edge EXAFS spectrum in Figure 8b, together with the related fitting curve, we verified that the structure of fresh 70Co\_MHS before the FTS reaction is well consistent with that of Co<sub>3</sub>O<sub>4</sub>. Table 3 shows three different coordination distances at 1.93, 2.88 and 3.39 Å for first (Co-O), second (Co-Co) and third (Co-Co) shells, respectively. Meanwhile, the corresponding coordination numbers are in the range of 5.0–6.2. The above *R* and CN values are in good agreement with those in Co<sub>3</sub>O<sub>4</sub> models (see Table 3).

For the used catalysts after FTS, besides 70Co\_MHS, we used 30Co as a comparison. From XANES profiles in Figure 8c, as well as the related linear combination fits in Figure 9, we can determine that the used 30Co/Al was consisted of 30%Co + 70%CoO, identical to Co<sup>1.4</sup>; while the used 70Co\_MHS was composed by 53%Co + 47%CoO, very close to Co<sup>0.9</sup>. Thus, cobalt in 70Co\_MHS was more reduced than that in 30Co after FTS. The corresponding EXAFS spectra with fits in Figure 8d determine both Co-O and Co-Co contributions in either 30Co or 70Co\_MHS after the reaction. Furthermore, the Co-Co shell around 2.5 Å is more dominant for 70Co\_MHS than that for 30Co, confirming the above linear combination fit results in XANES. From Table 3, we can see that the local coordination structure of used 70Co\_MHS or 30Co is the mixture of Co and CoO phases. Specifically, the Co-O (~ 2 Å) and Co-Co (~ 3 Å) shells belong to CoO, while the Co-Co (~ 2.5 Å) is assigned to metallic Co. Distinctly, the Co-Co metallic bond in the used 70Co\_MHS has higher CN value than that in the used 30Co (4.8 vs 2.2), giving an hint that the mesoporous hollow structure contained more fraction of crystallized Co metals than the solid sphere after the FTS reaction. Therefore, the catalytic performance of Co<sub>3</sub>O<sub>4</sub>-Al<sub>2</sub>O<sub>3</sub> catalysts for FTS could be caused by the metallic Co component, and the stabilization of such active species could be due to the formation of mesoporous hollow sphere with interfacial alumina, which may maximize the cobalt skeleton in synthesis compared to the counterparts with other Co/Al ratios.

Additionally, we have done the nearly *in-situ* investigation of 70Co\_MHS by XRD technique. As XRD patterns shown in Figure 10, traced phase transformation of 70Co\_MHS revealed the Co<sub>3</sub>O<sub>4</sub> changed to CoO during pre-treatment (350 °C, 5%H<sub>2</sub>) and preserved at reaction condition (220 °C, 33.3%CO + 66.6%H<sub>2</sub>). No crystallized metallic Co could be detected during the whole

process. However, as proved by the *ex-situ* characterization (XAFS, Figure 8c and 8d), abundant metallic Co was present after FTS reaction. Thus, we can speculate the  $\text{Co}^0$  species might be formed with highly disordered nature during reaction.

Temperature-programmed reduction by hydrogen ( $\text{H}_2$ -TPR) and the corresponding *in-situ* XRD analysis were conducted to investigate the correlation between the redox behavior and the catalytic performance over both mesoporous hollow structure and solid sphere. Figure 11a exhibits two  $\text{H}_2$ -TPR peaks are centered at ca. 390 and 600 °C for 70Co\_MHS; while higher reduction temperatures (ca. 480 and 630 °C) appear for 30Co, indicating that 70Co\_MHS is easier to be reduced than 30Co. On the basis of the *in-situ* XRD results in Figure 11b, the stepwise reductions of  $\text{Co}_3\text{O}_4 \rightarrow \text{CoO}^{[49]}$  and sequential  $\text{CoO} \rightarrow \text{Co}^{[49]}$  happened for 30Co, and the final phase at 800 °C was the combination of Co and CoO. However, for 70Co\_MHS, owing to the complete transform from CoO to Co, pure metallic cobalt structure was created at 800 °C (Figure 11c). Additionally, as displayed in Figure S3b, abundant amorphous alumina is placed at the surround area of  $\text{Co}_3\text{O}_4$  particles for 30Co with strong interaction, and which was also proved by the dominate Co 2p peak (Figure S12) located at 781.6 eV (1.4 eV higher than 70Co\_MHS) with characteristic gap (15.7 eV) and strong shake-up satellite, indicating the dominate formation of hardly reduced cobalt aluminate in 30Co.<sup>[36,50]</sup> Therefore, these data verify that the 70Co\_MHS with moderate interaction was easier to be reduced than these strongly interacted with ambient alumina (e.g. 30Co).

#### 4. Conclusion

In this work, we have demonstrated a facile route to fabricate mixed metal oxides ( $\text{Co}_3\text{O}_4\text{-Al}_2\text{O}_3$ ) mesoporous hollow spheres via an aerosol-assisted self-assembly approach. The well-defined hollow microspheres are comprised by cobalt oxide particles with an average size of ca. 8 nm, plus the interfacial amorphous alumina. Systematic investigations on the formation of MHS identified that the diffusion of gaseous nitrogen oxides released during the pyrolysis of metal nitrates precursors, as well as the particular fraction of amorphous  $\text{Al}_2\text{O}_3$  played a crucial role as scaffold of the inside cavity. Meanwhile, the skeleton of  $\text{Co}_3\text{O}_4$  nanocrystals, as well as the adhesive effect of

non-crystalline Al<sub>2</sub>O<sub>3</sub> species, were found to stabilize such hollow structure. Owing to the unique MHS feature, the Co<sub>3</sub>O<sub>4</sub>-Al<sub>2</sub>O<sub>3</sub> nanocomposite showed superior catalytic performance in both reactivity and selectivity of desirable products for the Fischer-Tropsch synthesis reaction.

## 5. Author Information

Corresponding Author

jiacj@sdu.edu.cn; sirui@sinap.ac.cn; yan@pku.edu.cn

Notes

The authors declare no competing financial interest.

## 6. Acknowledgment

Financial supported from the Excellent Young Scientists Fund from National Science Foundation of China (NSFC, grant nos. 21622106), other projects from NSFC (grant nos. 21301107, 21373259, 21331001 and 21501109), the Taishan Scholar Project of Shandong Province (China), the Hundred Talents project of the Chinese Academy of Sciences, Doctoral Funding of Ministry of Education of China (grant nos. 20130131120009), Doctoral Funding of Shandong Province of China (grant nos. BS2014CL008), Open Funding from State Key Laboratory of Material Processing and Die & Mold Technology at Huazhong University of Science and Technology (P2014-10), the Strategic Priority Research Program of the Chinese Academy of Sciences (grant no. XDA09030102).

## 7. References

- [1] T. O. Eschemann, K. P. de Jong, *ACS Catal.* 5 (2015) 3181–3188.
- [2] J. C. Kang, K. Cheng, L. Zhang, Q. H. Zhang, J. S. Ding, W. Q. Hua, Y. C. Lou, Q. G. Zhai, Y. Wang, *Angew. Chem. Int. Ed.* 50 (2011) 5200–5203.
- [3] G. R. Johnson, A. T. Bell, *ACS Catal.* 6 (2016) 100–114.
- [4] J. C. Kang, S. L. Zhang, Q. H. Zhang, Y. Wang, *Angew. Chem. Int. Ed.* 48 (2009) 2565–2568.
- [5] H. M. Torres Galvis, J. H. Bitter, C. B. Khare, M. Ruitenbeek, A. I. Dugulan, K. P. de Jong, *Science* 335 (2012) 835–838.

- [6] K. Xu, B. Sun, J. Lin, W. Wen, Y. Pei, S. R. Yan, M. H. Qiao, X. M. Zhang, B. N. Zong, *Nat. Commun.* 5 (2014) 5783.
- [7] C. Yang, H. B. Zhao, Y. L. Hou, D. Ma, *J. Am. Chem. Soc.* 134 (2012) 15814–15821.
- [8] Q. Yang, X. P. Fu, C.-J. Jia, C. Ma, X. Wang, J. Zeng, R. Si, Y. W. Zhang, C. H. Yan, *ACS Catal.* 6 (2016) 3072–3082.
- [9] Z. K. Sun, B. Sun, M. H. Qiao, J. Wei, Q. Yue, C. Wang, Y. H. Deng, S. Kaliaguine, D. Y. Zhao, *J. Am. Chem. Soc.* 134 (2012) 17653–17660.
- [10] W. Chen, Z. L. Fan, X. L. Pan, X. H. B, *J. Am. Chem. Soc.* 130 (2008) 9414–9419.
- [11] H. Wang, W. Zhou, J. X. Liu, R. Si, G. Sun, M. Q. Zhong, H. Y. Su, H. B. Zhao, J. A. Rodriguez, S. J. Pennycook, J. Idrobo, W. X. Li, Y. Kou, D. Ma, *J. Am. Chem. Soc.* 135 (2013) 4149–4158.
- [12] Q. Yuan, A. X. Yin, C. Luo, L. D. Sun, Y. W. Zhang, W. T. Duan, Liu, H. C. C. H. Yan, *J. Am. Chem. Soc.* 130 (2008) 3465–3472.
- [13] Q. Yuan, H. Duan, L. Li, Z. Li, W. Duan, L. Zhang, W. Song, C. Yan, *Adv. Mater.* 22 (2010) 1475–1478.
- [14] G. H. Wang, J. Hilgert, F. H. Richter, F. Wang, *Nat. Mater.* 13 (2014) 293–300.
- [15] H. Liang, Y. Zhang, Y. Liu, *J. Rare Earths* 28 (2009) 425–430.
- [16] Q. Q. Hao, Z. W. Liu, B. S. Zhang, G. W. Wang, C. Ma, W. Frandsen, J. J. Li, Z. T. Liu, Z. P. Hao, D. S. Su, *Chem. Mater.* 24 (2012) 972–974.
- [17] D. Gu, C.-J. Jia, C. Weidenthaler, H. Bongard, B. Spliethoff, W. Schmidt, F. Schüth, *J. Am. Chem. Soc.* 137 (2015) 11407–11408.
- [18] G. D. Moon, J. B. Joo, M. Dahl, H. Jung, Y. D. Yin, *Adv. Funct. Mater.* 24 (2014) 848–856.
- [19] Y. X. Wang, J. P. Yang, S. L. Chou, H. K. Liu, W. X. Zhang, Y. D. Zhao, S. X. Dou, *Nat. Commun.* 68 (2015) 689.
- [20] Z. K. Sun, B. Sun, M. H. Qiao, J. Wei, Q. Yue, C. Wang, Y. H. Deng, S. Kaliaguine, D. Y. Zhao, *J. Am. Chem. Soc.* 134 (2012) 17653–17660.
- [21] W. Chen, Z. L. Fan, X. L. Pan, X. H. Bao, *J. Am. Chem. Soc.* 130 (2008) 9414–9419.
- [22] J. C. Zhao, Y. Yang, Z. C. Zhang, X. B. Xu, X. Wang, *J. Mater. Chem. A* 2014, 2, 20182–20188.

- [23] T. S. Deng, F. Marlow, *Chem. Mater.* 24 (2012) 536–542.
- [24] P. M. Arnal, C. Weidenthaler, F. Schüth, *Chem. Mater.* 18 (2006) 2773–2739.
- [25] D. T. Nguyen, K. Kim, *Chem. Eng. J.* 286 (2016) 266–271.
- [26] A. Cabot, M. Ibáñez, P. Guardia, A. P. Alivisatos, *J. Am. Chem. Soc.* 131 (2009) 11326–11328.
- [27] Y. D. Yin, R. M. Rioux, C. K. Erdonmez, S. Hughes, G. A. Somorjai, A. P. Alivisatos, *Science* 304 (2004) 711–714.
- [28] L. Shen, L. Yu, X. Yu, X. Zhang, X. W. Lou, *Angew. Chem. Int. Ed.* 54 (2015) 1868–1872.
- [29] F. Zou, X. L. Hu, Z. Li, L. Qie, C. C. Hu, R. Zeng, Y. Jiang, Y. H. Huang, *Adv. Mater.* 26 (2014) 6622–6628.
- [30] Y. N. Zhang, K. S. Suslick, *Chem. Mater.* 27 (2015) 7559–7563.
- [31] C. W. Wang, Y. Wang, J. Graser, R. Zhao, F. Gao, M. J. O'Connell, *ACS Nano* 7 (2013) 11156–11165.
- [32] Z. Jin, F. Wang, F. Wang, J. X. Wang, J. C. Yu, J. F. Wang, *Adv. Funct. Mater.* 23 (2013) 2137–2144.
- [33] Z. Jin, M. D. Xiao, Z. H. Bao, P. Wang, J. F. Wang, *Angew. Chem. Int. Ed.* 51 (2012) 6406–6410.
- [34] Newville, M. J. *Synchrotron Radiat.* 8 (2001) 96–100.
- [35] B. Ravel, M. J. Newville, *Synchrotron Radiat.* 12 (2005) 537–541.
- [36] L. Ji, J. Lin, H. C. Zeng, *J. Phys. Chem. B* 104 (2000) 1783–1790.
- [37] R. Riva, H. Miessner, R. Vitali, G. D. Piero *Appl. Catal. A: General* 196 (2000) 111–123.
- [38] Y. H. Yang, F. J. DiSalvo, *Chem. Mater.* 24 (2012) 4406–4409.
- [39] Y. H. Choi, Y. J. Jang, H. Park, W. Y. Kim, Y. H. Lee, S. H. Choi, J. S. Lee *Appl. Catal. B: Environ.* 202 (2017) 605–610.
- [40] C. Ahn, H. M. Koo, J. M. Jo, H. Roh, J.-B. Lee, Y.-J. Lee, E. J. Jang, J. W. Bae *Appl. Catal. B: Environ.* 180 (2016) 139–149.
- [41] G. L. Bezemer, J. H. Bitter, H. P. C. E. Kuipers, H. Oosterbeek, J. E. Holewijn, X. D. Xu, F. Kapteijn, A. J. van Dillen, K. P. de Jong, *J. Am. Chem. Soc.* 128 (2006) 3956–3964.

- [42] D. D. Hibbitts, B. T. Loveless, M. Neurock, E. Iglesia. *Angew. Chem. Int. Ed.* 52 (2013) 12273–12278.
- [43] D. Schanke, S. Eri, E. Rytter, C. Aaserud, A. M. Hilmen, O. A. Lindvg, E. Bergene, A. Holmen, *Stud. Surf. Sci. Catal.* 147 (2004) 301–306.
- [44] J. P. den Breejen, P. B. Radstake, G. L. Bezemer, J. H. Bitter, V. Frøseth, A. Holmen, and K. P. de Jong, *J. Am. Chem. Soc.* 131 (2009) 7197–7203.
- [45] N. Fischer, E. van Steen, M. Claeys, *J. Catal.* 299 (2013) 67–80.
- [46] Y. Yamada, M. Mizutani, T. Nakamura, K. Yano, *Chem. Mater.* 22 (2010) 1695–1703.
- [47] Y. Zhang, M. Koike, R. Yang, S. Hinchiranan, T. Vitidsant, N. Tsubaki, *Appl. Catal. A Gen.* 292 (2005) 252–258.
- [48] R. Takahashi, S. Sato, T. Sodesawa, M. Yabuki, *J. Catal.* 200 (2001) 197–202.
- [49] Y. Q. Gu, X. P. Fu, P. P. Du, D. Gu, Z. Jin, Y. Y. Huang, R. Si, L. Q. Zheng, Q. S. Song, C.-J. Jia, C. Weidenthaler, *J. Phys. Chem. C* 119 (2015) 17102–17110.
- [50] H. F. Xiong, Y. H. Zhang, K. Y. Liew, J. L. Li, *J. Mole. Catal. A: Chemical* 231 (2005) 145–151.

**Table 1.** Crystal phase and morphology, BET specific surface area ( $S_{\text{BET}}$ ), pore volume ( $V$ ), pore diameter ( $D$ ) and particle size ( $d$ ) of the  $\text{Co}_3\text{O}_4\text{-Al}_2\text{O}_3$  samples.

Sample	Phase <sup>a</sup>	Morphology <sup>b</sup>	$S_{\text{BET}}^c$ ( $\text{m}^2\cdot\text{g}^{-1}$ )	$V_p^c$ ( $\text{cm}^3\cdot\text{g}^{-1}$ )	$D_p^c$ (nm)	$d^d$ (nm)	$d^e$ (nm)	$DOR^f$ (%)
15Co	–	Solid	231	0.34	4.9	–	–	0
30Co	$\text{Co}_3\text{O}_4$	Solid	173	0.38	7.0	–	9.4	0
50Co	$\text{Co}_3\text{O}_4$	Solid	142	0.28	6.3	$7.9\pm 1.7$	8.3	32
70Co_MHS	$\text{Co}_3\text{O}_4$	Hollow	95	0.60	18.8	$8.5\pm 1.7$	8.6	58
70Co (without F127)	–	Hollow	56	0.31	18.6	–	–	–
70Co_SG	$\text{Co}_3\text{O}_4$	Solid	–	–	–	–	23.7	25
90Co	$\text{Co}_3\text{O}_4$	Solid	64.3	0.33	11.8	–	15.5	–
100Co	$\text{Co}_3\text{O}_4$	Solid	28	0.27	22.8	20–120	32.4	–
20Co-IM	$\text{Co}_3\text{O}_4$	Solid	–	–	–	–	7.3	57

<sup>a</sup> Determined by XRD patterns.

<sup>b</sup> Determined by SEM images.

<sup>c</sup> Diameter of pore,  $D$ , determined by  $\text{N}_2$  adsorption/desorption experiments.

<sup>d</sup> Particle size,  $d$ , is based on statistic data from more than 100 particles in TEM images.

<sup>e</sup> Particle size,  $d$ , is determined by XRD patterns.

<sup>f</sup> Degree of reduction.

**Table 2.** Catalytic reactivity and selectivity of the Co<sub>3</sub>O<sub>4</sub>-Al<sub>2</sub>O<sub>3</sub> samples for FTS.

Samples	GHSV	CO	<sup>b</sup> CTY × 10 <sup>-5</sup>	<i>r</i> <sub>FTS</sub> × 10 <sup>-2</sup>	CO <sub>2</sub>	CH <sub>4</sub> <sup>c</sup>	C <sub>5</sub> -C <sub>12</sub> <sup>c</sup>	C <sub>5+</sub> <sup>c</sup>
	NmL·g <sub>cat</sub> <sup>-1</sup> ·h <sup>-1</sup>	conversion (%)	mol <sub>CO</sub> ·g <sub>Co</sub> <sup>-1</sup> ·s <sup>-1</sup>	mol <sub>CO</sub> ·g <sub>cat</sub> <sup>-1</sup> ·h <sup>-1</sup>	(%)		(wt.%)	
15Co <sup>a</sup>	7500	3.7	0.71	0.4	2.7	45.9	14.3	14.5
30Co <sup>a</sup>	7500	23.4	2.44	2.3	1.9	40.5	30.2	36.1
50Co <sup>a</sup>	7500	42.4	2.91	4.3	1.0	20.5	46.2	64.8
70Co_MHS <sup>a</sup>	7500	65.7	3.51	6.7	0.9	14.0	52.4	70.7
70Co (Sol-gel) <sup>a</sup>	7500	17.8	0.95	1.8	5.6	21.8	38.0	42.9
100 Co <sup>a</sup>	7500	5.5	0.20	0.6	1.1	29.2	20.9	24.2
50Co	17100	20.3	3.1	4.5	6.4	21.5	41.8	55.4
70Co_MHS	25700	31.1	5.5	10.4	3.7	15.9	47.5	67.7
20Co_IM	4200	20.6	1.6	1.2	6.7	17.4	46.8	65.7

<sup>a</sup> Reaction conditions:  $T = 220$  °C,  $m_{\text{catal.}} = 80$  mg,  $\text{H}_2/\text{CO} = 2/1$ , 2.0 MPa, 10 mL·min<sup>-1</sup>, time-on-stream of 5 h.

<sup>b</sup> Cobalt-time-yield (CTY) of FTS reaction.

<sup>c</sup> Based on carbon calculations for all hydrocarbons (excluding CO<sub>2</sub>).



**Table 3.** EXAFS fitting results (*R*: distance; CN: coordination number) on the Co<sub>3</sub>O<sub>4</sub>-Al<sub>2</sub>O<sub>3</sub> samples before and after FTS.

Sample	Co–O (1st shell)		Co–Co (2nd shell)		Co–Co (3rd shell)	
	<i>R</i> (Å)	CN	<i>R</i> (Å)	CN	<i>R</i> (Å)	CN
70Co_MHS (fresh)	1.93±0.01	5.7±0.6	2.88±0.01	5.0±1.4	3.39±0.02	6.2±1.8
70Co_MHS (used)	2.04±0.03	1.6±0.6	2.51±0.01	4.8±0.5	3.01±0.02	2.6±0.8
30Co (used)	2.00±0.01	2.4±0.5	2.51±0.01	2.2±0.5	3.02±0.02	1.7±0.8
Co (model)	–	–	2.509	12	–	–
CoO (model)	2.133	6	–	–	3.017	12
Co <sub>3</sub> O <sub>4</sub> (model)	1.943	6	2.874	6	3.370	6

## Figure Captions:

**Scheme 1.** Schematic illustration on the stepwise formation of  $\text{Co}_3\text{O}_4\text{-Al}_2\text{O}_3$  MHS.

**Figure 1.** a) SEM image, b) TEM image and c) STEM-EDS elemental line scanning of as-prepared 70Co\_MHS; d) TEM image (inserted is the statistical histogram on particle size), e) HRTEM image and e) STEM-EDS elemental area mapping of crushed 70Co\_MHS.

**Figure 2.** a) XRD pattern and b) Co 2p XPS profile of as prepared 70Co\_MHS.

**Figure 3.** TEM images of the  $\text{Co}_3\text{O}_4\text{-Al}_2\text{O}_3$  samples: a) 15Co; b) 30Co; c) 50Co; d) 100Co.

**Figure 4.** a) SEM image, b) STEM-EDS elemental line scanning, c) STEM-EDS elemental area mapping and d) XRD pattern of 70Co\_IM.

**Figure 5.** a) CO conversion (black, column) and cobalt-time-yield CTY (red, square) of the  $\text{Co}_3\text{O}_4\text{-Al}_2\text{O}_3$  samples; b) Products selectivity of the  $\text{Co}_3\text{O}_4\text{-Al}_2\text{O}_3$  samples. Reaction conditions: TOS = 5 h,  $\text{H}_2/\text{CO} = 2/1$ ,  $T = 220\text{ }^\circ\text{C}$ , 2 MPa, GMSV =  $7,500\text{ mL}\cdot\text{g}^{-1}\cdot\text{h}^{-1}$ .

**Figure 6.** a) Long-time test on 70Co\_MHS. b) Catalytic performance of 70Co\_MHS and 70Co (Sol-gel). Reaction conditions: TOS = 5 h,  $\text{H}_2/\text{CO} = 2/1$ ,  $T = 220\text{ }^\circ\text{C}$ , 2 MPa, GMSV =  $7,500\text{ mL}\cdot\text{g}^{-1}\cdot\text{h}^{-1}$ .

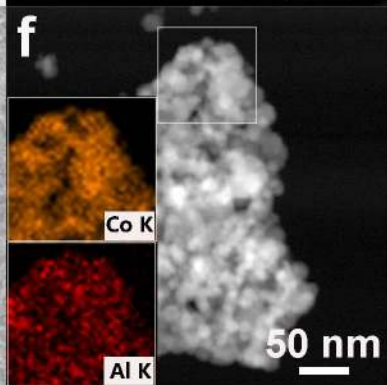
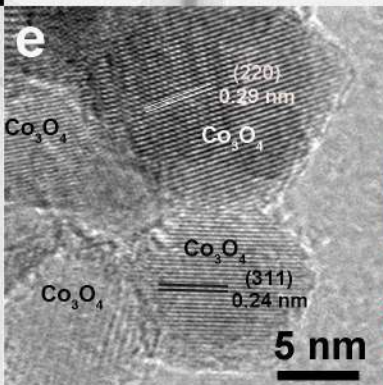
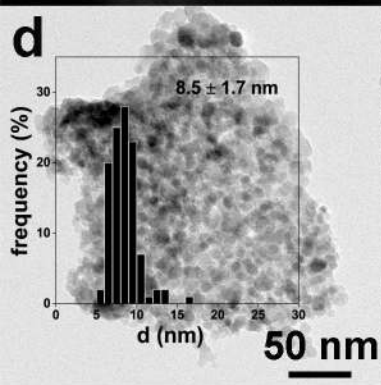
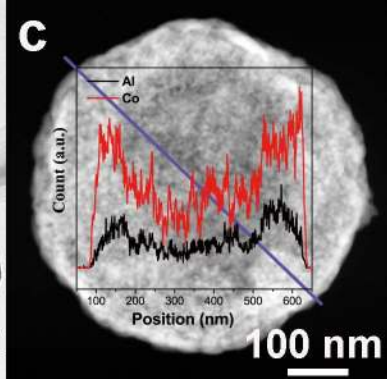
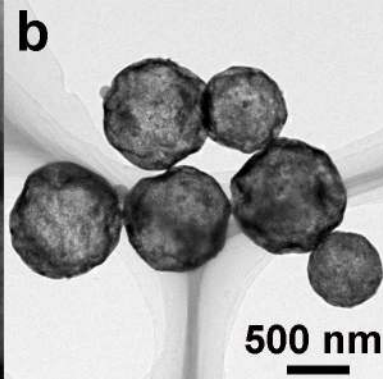
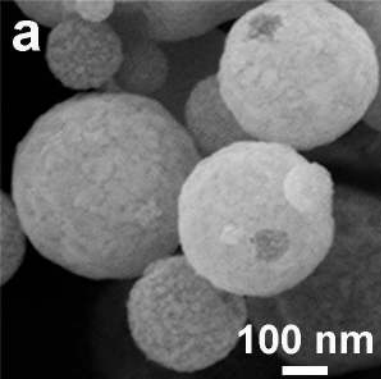
**Figure 7.** TEM images of catalysts after FTS reaction. a) 30Co used, b) 70Co\_MHS used and c) 100Co used.

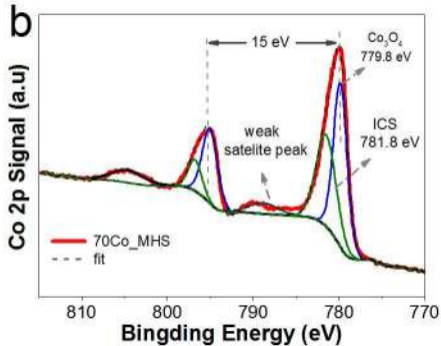
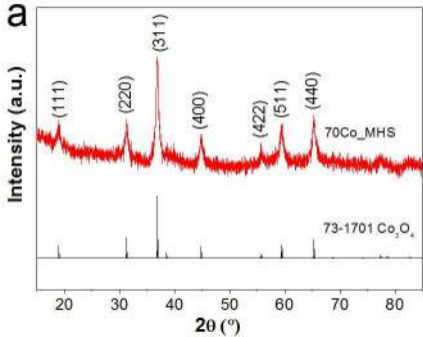
**Figure 8.** a,c) XANES profile and b,d) EXAFS spectra with fitting curves in R space for the  $\text{Co}_3\text{O}_4\text{-Al}_2\text{O}_3$  samples a,b) before and c,d) after FTS.

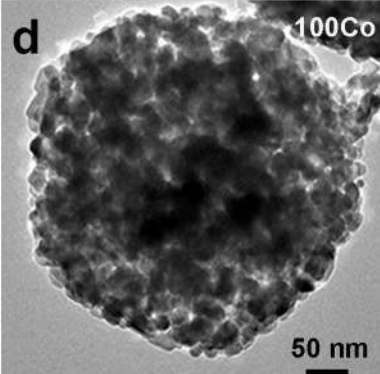
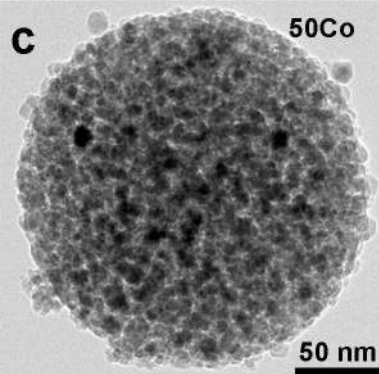
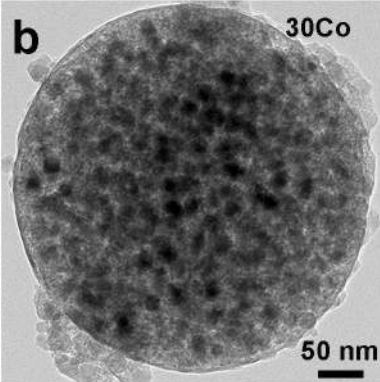
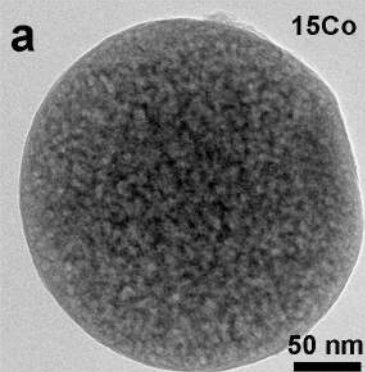
**Figure 9.** XANES liner combination fits on a) 30Co (used) and b) 70Co\_MHS (used).

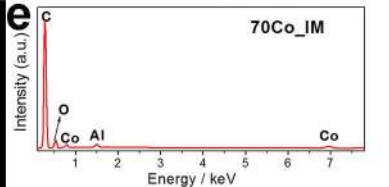
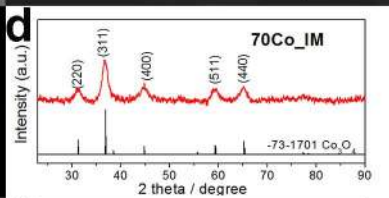
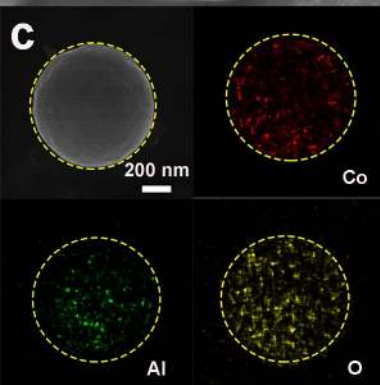
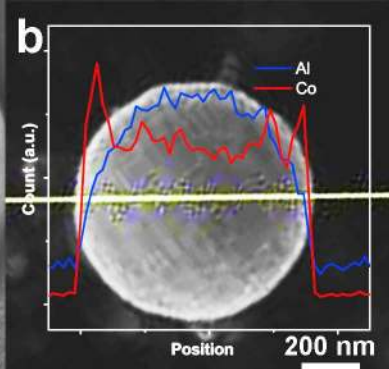
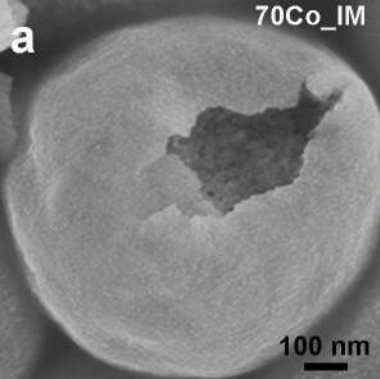
**Figure 10.** *In-situ* XRD patterns of 70Co\_MHS during various condition: a) 10%  $\text{H}_2/\text{Ar}$ , 50 mL/min,  $350\text{ }^\circ\text{C}$ . b) 33.3%  $\text{CO}/\text{H}_2$ , 15mL/min,  $220\text{ }^\circ\text{C}$ .

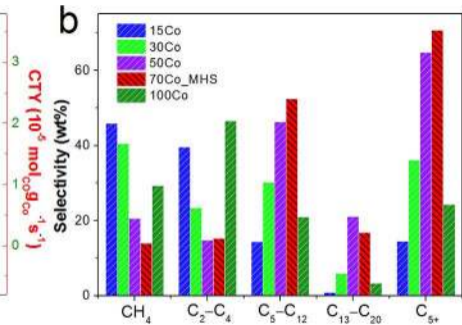
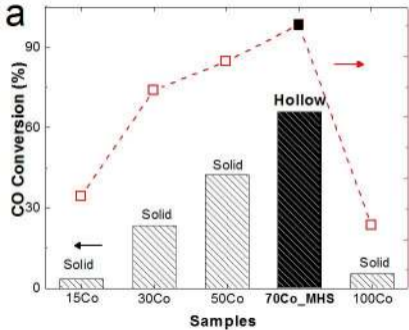
**Figure 11.** a)  $\text{H}_2$ -TPR profiles of the  $\text{Co}_3\text{O}_4/\text{Al}_2\text{O}_3$  samples; *In-situ* XRD patterns of b) 30Co and c) 70Co\_MHS under the same testing conditions as  $\text{H}_2$ -TPR.

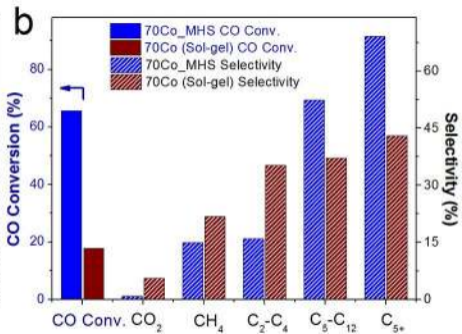
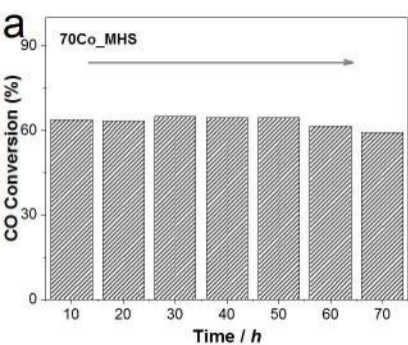




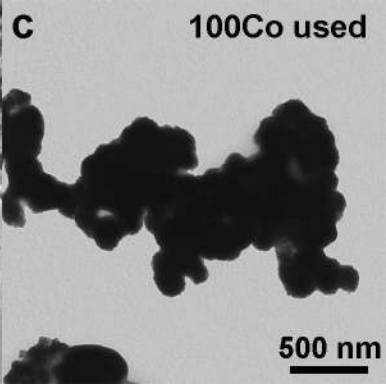
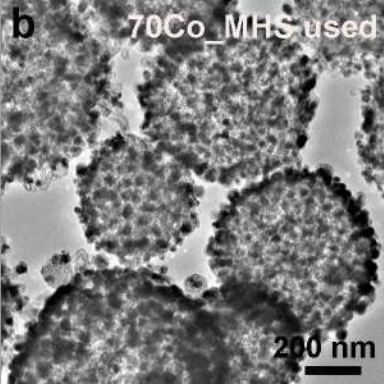
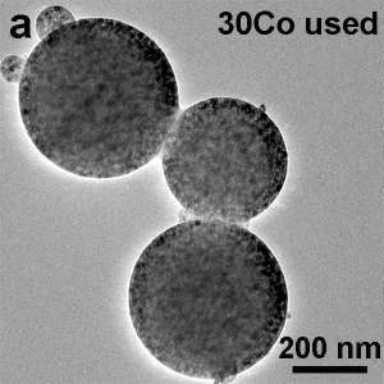


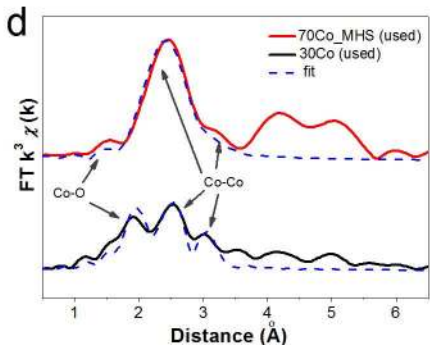
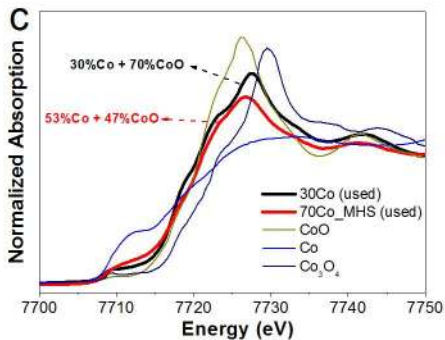
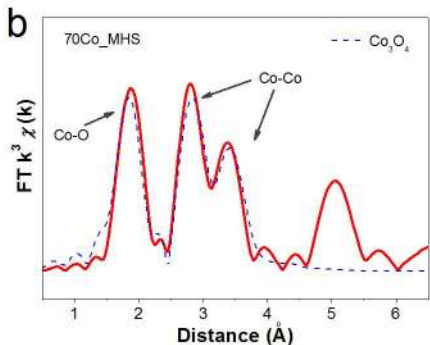
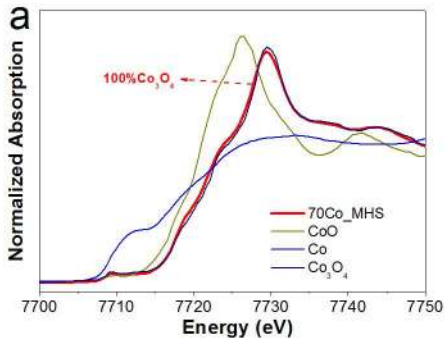


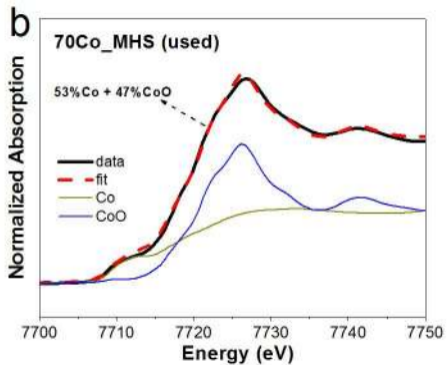
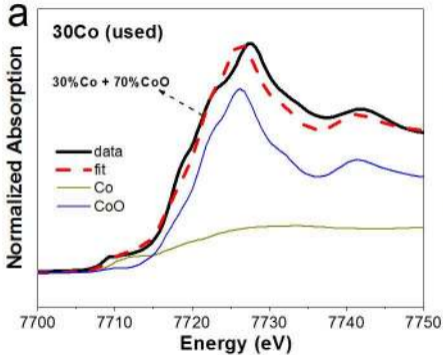


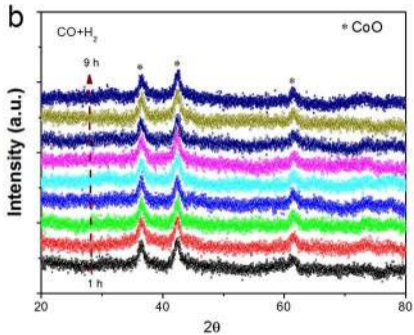
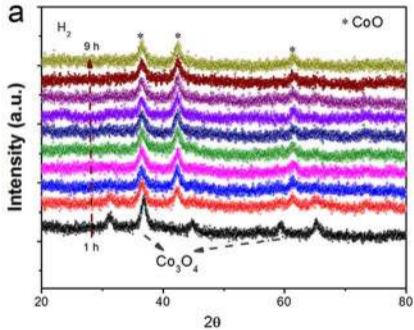


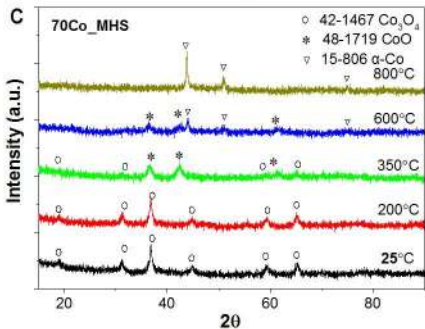
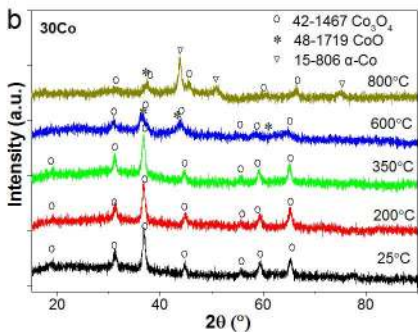
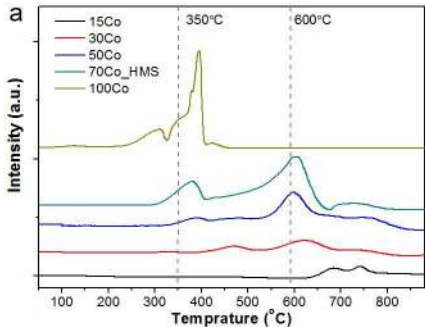












# **Co<sub>3</sub>O<sub>4</sub>-Al<sub>2</sub>O<sub>3</sub> Mesoporous Hollow Spheres as Efficient Catalyst for Fischer-Tropsch Synthesis**

Xin-Pu Fu<sup>a</sup>, Qi-Kai Shen<sup>a</sup>, Dong Shi<sup>a</sup>, Ke Wu<sup>c</sup>, Zhao Jin<sup>a</sup>, Xu Wang<sup>b</sup>, Rui Si<sup>\*.b</sup>,

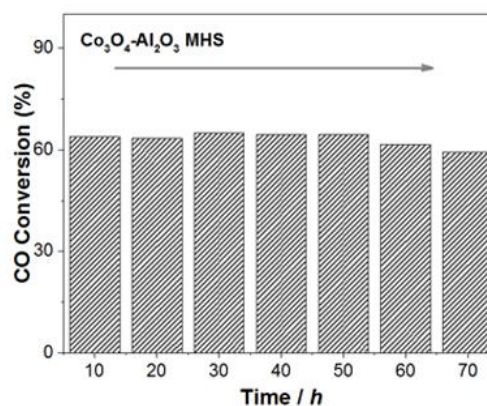
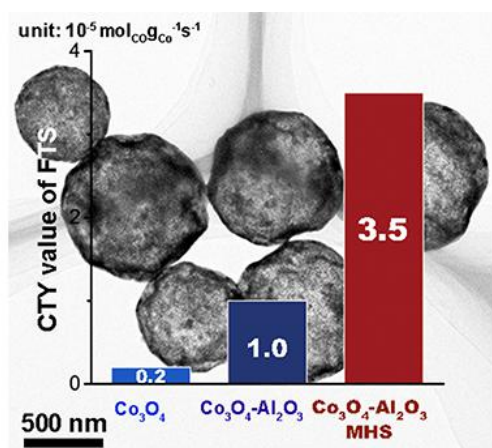
Qi-Sheng Song<sup>a</sup>, Chun-Jiang Jia<sup>\*.a</sup>, Chun-Hua Yan<sup>\*.c</sup>

<sup>a</sup>Key Laboratory for Colloid and Interface Chemistry, Key Laboratory of Special Aggregated Materials, School of Chemistry and Chemical Engineering, Shandong University, Jinan 250100, China

<sup>b</sup>Shanghai Synchrotron Radiation Facility, Shanghai Institute of Applied Physics, Chinese Academy of Sciences, Shanghai 201204, China

<sup>c</sup>Beijing National Laboratory for Molecular Sciences, State Key Lab of Rare Earth Materials Chemistry and Applications, PKU-HKU Joint Lab in Rare Earth Materials and Bioinorganic Chemistry, Peking University, Beijing 100871, China

## Graphical abstracts



Hollow architecture assembled by vast small  $\text{Co}_3\text{O}_4$  nanoparticles and bits interfacial  $\text{Al}_2\text{O}_3$  displays ample porosity and rational nanostructure. Accordingly, as a result of improved mass transfer property and optimized interaction between active sites and matrix, as-prepared  $\text{Co}_3\text{O}_4\text{-Al}_2\text{O}_3$  MHS exhibits much better performance in catalysis-energy application than traditional one.